Available online at www.sciencedirect.com
ScienceDirect
Ocean Modelling 16 (2007) 95–105
Ocean Modelling
www.elsevier.com/locate/ocemod

Spurious instabilities of long planetary waves in a two-and-a-half layer model subtropical gyre ocean with a wind-driven steady circulation

Ivana Cerovečki *,[1], Roland A. de Szoeke

College of Oceanic and Atmospheric Sciences, Oregon State University, 104 COAS Admin. Building, Corvallis, OR 97331-5503, USA

Received 29 April 2006; received in revised form 27 July 2006; accepted 28 July 2006
Available online 7 September 2006

Abstract

In a number of flows that support coupled free-waves, instability results when free-wave dispersion relations calculated without the coupling cross or approach one another. The propagation of long planetary wave perturbations of a two-and-a-half layer model subtropical gyre is one such oceanographically important instance. This note points out that, for a baroclinically unstable two-and-a-half layer model subtropical gyre, numerically aliased long wave dispersion relation plots display extra crossings that are artifacts of the discretization, and these may lead both to spurious numerical instabilities and to numerical misrepresentation of actual instabilities. Paradoxically, the numerical instability may in some instances manifest itself more strongly as the numerical resolution is improved. The aliasing mechanism may be related to the zone of small scale activity found in the southwestern corner of a time dependent model subtropical gyre in the numerical perturbation experiments of (Dewar, W., Huang, R., 2001. Adjustment of the ventilated thermocline. J. Phys. Oceanogr. 13, 293–309). Similar multilayer models are often discussed in the literature, so that the results may be widely useful.

Keywords: Spurious instabilities; Long planetary waves

1. Introduction

Pichevin (1998) points out that if the layers of a three layer quasigeostrophic model are dynamically isolated from one another so that Rossby waves propagate independently in each layer, then restoring the dynamical coupling between the layers leads to instabilties when the waves propagate at the same speed. Sakai (1989) finds a similar result in a different dynamical context. Cerovečki and de Szoeke (2005, in press) found that for time periodic perturbations of a two-and-a-half layer model subtropical gyre, spatial instability results

* Corresponding author.
E-mail address: ivana@rossby.mit.edu (I. Cerovečki).
[1] Present address: 54-1726 Department of Earth, Atmospheric, and Planetary Sciences, Massachusetts Institute of Technology, 77 Massachusetts Avenue, Cambridge, MA 02139-4307, USA.

1463-5003/$ - see front matter © 2006 Published by Elsevier Ltd.
doi:10.1016/j.ocemod.2006.07.004

when the two branches of the free-wave dispersion relation approach one another. This instability is similar to those found by Liu (1999a,b), who perturbed the steady flow of an eddy resolving three layer quasigeostrophic unventilated ocean model with Ekman pumping harmonic at periods of several years, and by Dewar and Huang (2001), who carried out similar experiments with a partially ventilated subtropical gyre flow.

This note points out that, in the numerical solution of the two-and-a-half layer model subtropical gyre perturbation problem, the numerically aliased long wave dispersion relations have extra crossings that are artifacts of the discretization, and that these as well as the usual truncation error may lead both to spurious numerical instabilities and to numerical misrepresentation of actual instabilities. The numerical instability may in some instances manifest itself more strongly as the numerical resolution is improved. Similar multilayer models are often discussed in the literature, so that the results may be useful beyond the present example.

2. Model equations

The time periodic (radian frequency σ) perturbations ξ_1 and ξ_2 of the upper and lower interfaces of the eastern shadow zone of a two-and-a-half layer ventilated thermocline model (Luyten et al., 1983) associated with linear free planetary waves are governed by

$$\phi_x = \mathrm{i}\sigma\xi_{2x}, \quad U_\mathrm{R}\xi_{2x} + V_\mathrm{R}\xi_{2y} = \mathrm{i}\sigma[(1 + c/C)\xi_2 + \phi/C] \tag{1}$$

(the beta plane version of Eq. (2.4) of Kubokawa and Nagakura, 2002) in which $\phi \equiv -c\xi_2 - C\xi_1$. In these equations and subsequently, subscripts x and y denote differentiation. For notational simplicity we employ the abbreviations

$$C(x,y) \equiv \frac{\beta\gamma_1 H_1^0}{f^2}, \quad c(y) \equiv \frac{\beta\gamma_2 H_2^0}{f^2} \tag{2}$$

where f is the usual Coriolis parameter with meridional derivative β, H_j^0 is the unperturbed depth of the base of layer j (indices $j = 1, 2$ correspond to the upper and middle layer), the γ_j are reduced gravity parameters $\gamma_j = g(\rho_{j+1} - \rho_j)/\rho_0$ with ρ_j the density of layer j, ρ_0 the mean density and g the acceleration of gravity. In terms of these

$$U_\mathrm{R} \equiv \frac{\gamma_2}{\gamma_1}(u_\mathrm{g} + c_\mathrm{R}), \quad V_\mathrm{R} \equiv \frac{\gamma_2}{\gamma_1} v_\mathrm{g}, \tag{3}$$

where u_g, v_g are the mean upper layer geostrophic velocity components $-\gamma_1 H_{1y}^0/f$ and $\gamma_1 H_{1x}^0/f$ in the zonal x and meridional y directions and $c_\mathrm{R} = C - \frac{\gamma_1}{\gamma_2}c$.

The WKB dispersion relation for free plane wave solutions $\mathrm{e}^{-\mathrm{i}(\sigma t - kx - ly)}$ of (1) is

$$\sigma^2 + \sigma(c + C)k - CU_\mathrm{R}k^2 - CV_\mathrm{R}kl = 0. \tag{4}$$

The properties of free solutions with dispersion relation (4) have already been discussed by Liu (1999a,b) and by Kubokawa and Nagakura (2002). Fig. 1 shows this dispersion relation for annual period waves at a particular location in the eastern shadow zone of the mean flow. For sufficiently small meridional scales (large $|l|$), there are two distinct dispersion curves. These correspond to the Non-Doppler-shift mode N and advective mode A of Liu (1999a), which reduce to the first (fast) and second (slow) baroclinic mode in the case of no background flow. These curves approach one another over a limited range of values of l, negative in the particular case of Fig. 1 and generally negative over most of the model subtropical gyre where $V_\mathrm{R} < 0$, within which spatial instability (complex zonal wavenumber k) occurs.

3. Solution by integration along characteristics

The governing Eq. (1) are hyperbolic in x, y with characteristics given by

$$\mathrm{d}y/\mathrm{d}x = \begin{cases} 0 \\ V_\mathrm{R}/U_\mathrm{R} \end{cases} \tag{5}$$

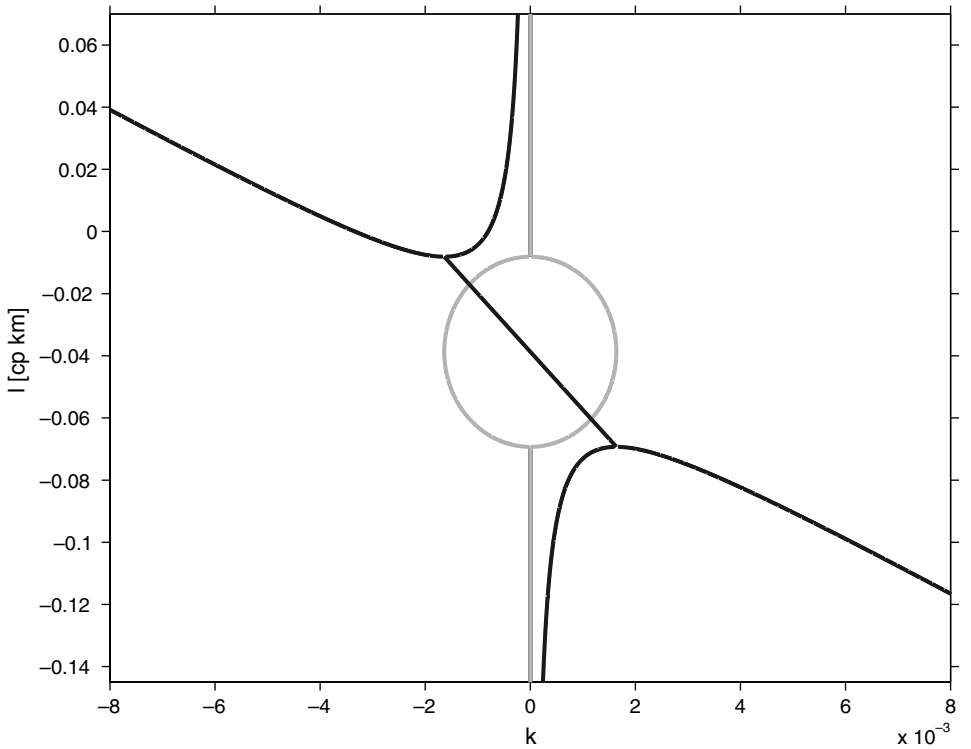

Fig. 1. The dispersion relation (4) for parameters c, C, U_R and V_R at a location $x = 9000$ km, $y = 2500$ km in the steady subtropical gyre flow that is driven by steady Ekman pumping of amplitude W_0 having the form $w_E^{(0)}(y) = -W_0\left(\frac{f_0}{f}\right)^2 \sin\left[\frac{(y-b)\pi}{\Delta}\right]$ in which f_0 is the Coriolis parameter at the central latitude $y = b$ of a basin of meridional extent $\Delta = 3000$ km whose eastern boundary is at $x = a$ (10,000 km). The dispersion relation is obtained by assuming real meridional wavenumber l and solving (4) for the zonal wavenumber k (real values plotted as heavy lines, imaginary values plotted as light lines). Note that k is real except over a restricted range of meridional wavenumber l. For this range of l, corresponding solutions of (1) grow zonally. Numerical values of parameters are $U_R = -1.4 \times 10^{-2}$ m/s, $V_R = -0.996 \times 10^{-4}$ m/s, $c = C = 0.0243$ m/s, $a = 10{,}000$ km, and the strength of the Ekman pumping W_0 is chosen so that the total transport in the model subtropical gyre is 22 Sv.

and shown in Fig. 2a. Analytic or numerical integration along characteristics is a widely used method of solution for hyperbolic problems such as the frequently employed layered thermocline model of Luyten et al. (1983) (for which the steady flow about which we perturb in this paper is the simplest example) or for shallow water problems. The one-dimensional nonlinear shallow water initial value problem governing horizontal velocity $u(x,t)$ and free surface elevation $\zeta(x,t)$ may also be reduced to a pair of coupled, hyperbolic first order equations $(\partial_t + (u \pm c)\partial_x)(u \pm 2c) = 0$ in which the shallow water wave speed c is given by $c^2 = g(H + \zeta)$ where H is the undisturbed fluid depth. These equations may be time stepped numerically along the characteristics $\mathrm{d}x/\mathrm{d}t = u \pm c$ from an initial specification of $u(x,0)$ and $c(x,0)$ to build up values of the Riemann invariants $(u \pm 2c)$ at an irregular grid of points in x,t (e.g. Stoker, 1957).

We initially applied the same procedure to solutions of (1), integrating along the characteristics defined by (5), but found it difficult to maintain sufficient zonal resolution in the southwest corner of the subtropical gyre on account of the tendency of the two families of characteristics to become ever more nearly parallel as the integration progressed further westward. Yet the idea of integrating along characteristics remained attractive because (i) the equations form a system of coupled ordinary differential equations in a parameter varying along the characteristics, allowing a simple march along the characteristics, and (ii) the resulting grid preserves the zone of influence westward of an isolated patch of wind stress or of boundary forcing.

We therefore decided to carry out the westward integration along all characteristics simultaneously using the adaptive Runge–Kutta procedures provided in Matlab to always retain sufficient zonal resolution. This however necessitated interpolating the variable stepped forward along each set of characteristics to the other

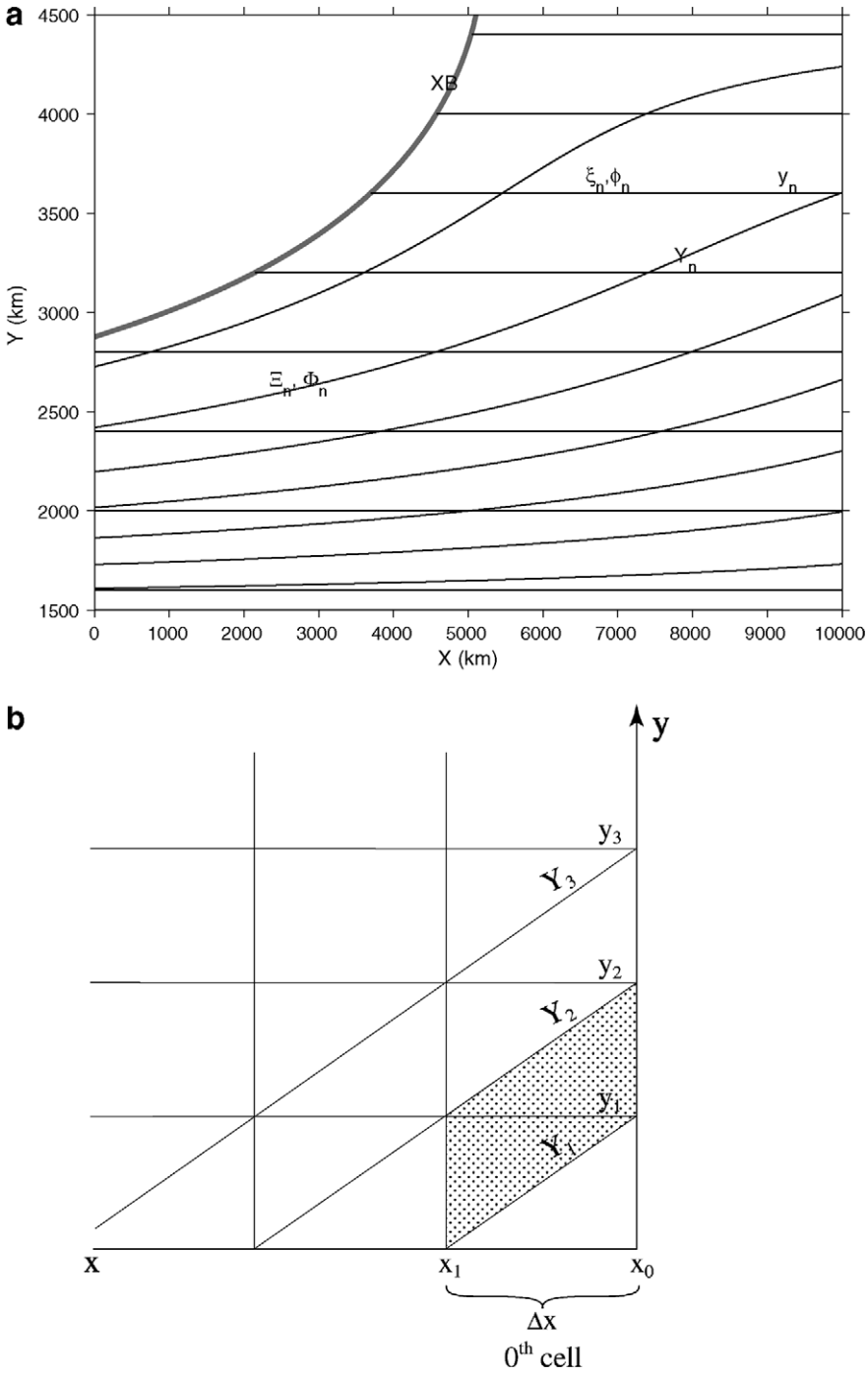

Fig. 2. Top panel: The two sets of eastern shadow zone characteristics $\mathrm{d}y(x;y_0)/\mathrm{d}x = 0$ where $y(a;y_0)_n = y_{0_n}$, and $\mathrm{d}Y(x;y_0)/\mathrm{d}x = V_\mathrm{R}/U_\mathrm{R}$ where $Y(a;y_0)_n = y_{0_n}$ (y_{0_n} is the meridional location at which a characteristic labeled n strikes the basin eastern boundary at $x = a$). The westernmost characteristic $Y(x;b + \Delta/2)$ that strikes the eastern boundary at the northeast corner of the basin is the western boundary $x = x_\mathrm{B}(y)$ of the eastern shadow zone. The variables ξ and ϕ are notated ξ_n and ϕ_n on the y_n and Ξ_n and Φ_n on the Y_n. Bottom panel: The eastern shadow zone characteristics $y(x;y_0)$ and $Y(x;y_0)$, idealized as straight lines for the von Neumann stability analysis. (Note that as explained in text, actual computations were carried out using the stretched coordinate χ rather than x.)

set. Various interpolation schemes (linear, cubic, spline) were tried. The final results were obtained using cubic interpolation, spline interpolation gave very similar results. The procedure was as follows. We denote the set

of characteristics obeying $\mathrm{d}y/\mathrm{d}x = 0$ by $y(x;y_0)$ where $y(a;y_0) \equiv y_0$, and the set obeying $\mathrm{d}y/\mathrm{d}x = V_\mathrm{R}/U_\mathrm{R}$ by $Y(x;y_0)$ where $Y(a;y_0) = y_0$ (in both of which y_0 is the originating latitude of a characteristic at the eastern boundary $x = a$). At each Runge–Kutta step, the variables ξ_2 and ϕ must be interpolated from one set of the characteristics to the other. We notate these variables in lower case along $\mathrm{d}y/\mathrm{d}x = 0$ as ξ (hereafter dropping the subscript 2) and ϕ, and in upper case along $\mathrm{d}y/\mathrm{d}x = V_\mathrm{R}/U_\mathrm{R}$ as Ξ and Φ (Fig. 2a). The two sets of Eq. (1) can be schematically written as

$$\left.\frac{\mathrm{d}}{\mathrm{d}x}\phi_n(x)\right|_y = \mathrm{i}\sigma\xi_n(x) \quad n = 1, 2, \ldots, N \tag{6}$$

$$\left.\frac{\mathrm{d}}{\mathrm{d}x}\Xi_n(x)\right|_Y = \mathrm{i}\sigma\left[\hat{d}\Xi_n(x) + \hat{c}\Phi_n(x)\right] \quad n = 1, 2, \ldots, N \tag{7}$$

Here, $\hat{d} = (c + C)/(CU_\mathrm{R})$ and $\hat{c} = 1/(CU_\mathrm{R})$, and the dependent variables have been discretized in the y direction so that the subscripts n index the respective characteristics. For simplicity of exposition only, the numbers N of zonal and tilted characteristics have been taken equal here and subsequently.

The westernmost characteristic satisfying $\mathrm{d}y/\mathrm{d}x = V_\mathrm{R}/U_\mathrm{R}$ is the western boundary $x = x_\mathrm{B}(y)$ of the eastern shadow zone of the mean flow. It is convenient in numerical integration to introduce a stretched meridional coordinate $\chi \equiv a\ \log((x_\mathrm{B}(y) - x)/(x_\mathrm{B}(y) - a))$ that removes the western boundary $x = x_\mathrm{B}(y)$ of the eastern shadow zone to $\chi = -\infty$. All the results that follow have been obtained in χ, y coordinates but are presented in the corresponding x, y coordinates.

4. Stability analysis

To examine the properties of this discrete numerical scheme, an extension of the classical von Neumann analysis of the numerical scheme was performed for free-waves. The coefficients c, C, U_R, V_R are assumed locally constant, so that each set of characteristics is a set of parallel straight lines, one zonal and one with slope $V_\mathrm{R}/U_\mathrm{R}$. For simplicity we assume that the number N of both types of characteristics is the same and that both sets of characteristics are meridionally equally spaced with the increment Δy. The coefficients $\hat{d}$ and $\hat{c}$ appearing in (7) are thus constant. Ultimately, the numerical dispersion relation for free-waves will be compared to the WKB dispersion relation (4).

The two sets of characteristics divide the x, y plane into a periodically repeating pattern of identical cells (Fig. 2b). The x coordinates of the southeast and southwest corners of the jth cell are denoted by x_j and x_{j+1}, respectively with $j = 0$ at the eastern boundary (though x increases towards the east, the indices of the cells increase westward, since that is the sense of propagation of long PG waves and therefore of the numerical integration). The zonal width of the cell is given by $\Delta x = x_j - x_{j+1}$. When working within cell j it is convenient to define $\tau_j = (x_j - x)/\Delta x$. Each Runge–Kutta step yields Ξ on the set of Y characteristics (tilted lines) and ϕ on the set of y characteristics (zonal lines). To again step Eq. (6) forward, values of ξ must be obtained by interpolating values of Ξ from the tilted characteristics to the zonal ones, while to again step Eq. (7) forward, values of Φ must be obtained by interpolating values of ϕ from the zonal characteristics to the tilted ones. For example, if linear interpolation among nearest neighbors is used, then within the jth cell,

$$\xi_n = (1 - \tau_j)\Xi_{n+j} + \tau_j\Xi_{n+j+1}, \tag{8}$$

$$\Phi_n = (1 - \tau_j)\phi_{n-j} + \tau_j\phi_{n-j-1}. \tag{9}$$

Higher order interpolation, involving more points than nearest neighbors, and therefore nonlinear (e.g., cubic) dependence on τ_j can be readily handled.

In the spirit of the von Neumann analysis, we seek discrete solutions trigonometric in y and Y. Consider one Fourier constituent (meridional wavenumber l) at a time

$$\Xi_n = \widetilde{\Xi}^{(j)}(x, l)\mathrm{e}^{\mathrm{i}l(n+j)\Delta y}, \quad \phi_n = \tilde{\phi}(x, l)\mathrm{e}^{\mathrm{i}ln\Delta y}. \tag{10}$$

Use the interpolation formulae (8) and (9) to write the system defined by (6) and (7) in terms of $\widetilde{\Xi}^{(j)}$ and $\tilde{\phi}$ only, to obtain

$$\left.\frac{\mathrm{d}}{\mathrm{d}x}\tilde{\phi}(x,l)\right|_y = \mathrm{i}\sigma f(\tau_j)\widetilde{\Xi}^{(j)}(x,l), \tag{11}$$

$$\left.\frac{\mathrm{d}}{\mathrm{d}x}\widetilde{\Xi}^{(j)}(x,l)\right|_Y = \mathrm{i}\sigma[\hat{d}\widetilde{\Xi}^{(j)}(x,l) + \hat{c}f^*(\tau_j)\tilde{\phi}(x,l)]. \tag{12}$$

Here $f(\tau) = (1-\tau) + \tau \mathrm{e}^{\mathrm{i}l\Delta y}$ denotes the interpolation function, and $f^*(\tau)$ its complex conjugate. Since $\mathrm{d}\tau_j = -\mathrm{d}x/\Delta x$, (11) and (12) become (dropping the j labels)

$$\frac{1}{\Delta x}\frac{\mathrm{d}}{\mathrm{d}\tau}\begin{pmatrix}\tilde{\phi}\\ \widetilde{\Xi}\end{pmatrix} = -\mathrm{i}\sigma\begin{pmatrix}0 & f\\ \hat{c}f^* & \hat{d}\end{pmatrix}\begin{pmatrix}\tilde{\phi}\\ \widetilde{\Xi}\end{pmatrix}, \quad 0 \leqslant \tau \leqslant 1. \tag{13}$$

Concentrating on one cell at a time, we seek to express the solution at the western edge of the cell ($\tau = 1$), as a function of the solution at the eastern edge of the cell ($\tau = 0$). Because the coordinate $\tau_j = \frac{(x_j - x)}{\Delta x}$ appears in the elements of the right hand side of (13), the integration across a cell must be performed numerically. The solution $\tilde{\phi}(\tau)$, $\widetilde{\Xi}(\tau)$ is expressed as a linear combination of two independent solutions φ_1, ξ_1 and φ_2, ξ_2 of (13)

$$\left.\begin{pmatrix}\tilde{\phi}\\ \widetilde{\Xi}\end{pmatrix}\right|_\tau = A\begin{pmatrix}\varphi_1(\tau)\\ \zeta_1(\tau)\end{pmatrix} + B\begin{pmatrix}\varphi_2(\tau)\\ \zeta_2(\tau)\end{pmatrix}. \tag{14}$$

If the boundary conditions at the eastern edge of the cell are $\varphi_1(0) = 1$, $\zeta_1(0) = 0$, $\varphi_2(0) = 0$, $\zeta_2(0) = 1$, then

$$\left.\begin{pmatrix}\tilde{\phi}\\ \widetilde{\Xi}\end{pmatrix}\right|_{\tau=1} = \begin{pmatrix}\varphi_1(1) & \varphi_2(1)\\ \zeta_1(1) & \zeta_2(1)\end{pmatrix}\left.\begin{pmatrix}\tilde{\phi}\\ \widetilde{\Xi}\end{pmatrix}\right|_{\tau=0}. \tag{15}$$

When the boundary between the two cells is crossed, both ϕ and Ξ must be continuous. The latter requirement applied to (10) shows that

$$\widetilde{\Xi}^{(j+1)} = \widetilde{\Xi}^{(j)}\mathrm{e}^{\mathrm{i}l\Delta y} \tag{16}$$

at $\tau_j = 1 + \epsilon$, $\tau_{j+1} = 0 - \epsilon$ which gives the matching condition

$$\left.\begin{pmatrix}\tilde{\phi}\\ \widetilde{\Xi}\end{pmatrix}\right|_{\tau_{j+1}=0-\epsilon} = \begin{pmatrix}1 & 0\\ 0 & \mathrm{e}^{\mathrm{i}l\Delta y}\end{pmatrix}\left.\begin{pmatrix}\tilde{\phi}\\ \widetilde{\Xi}\end{pmatrix}\right|_{\tau_j=1+\epsilon}. \tag{17}$$

A propagation matrix, relating the solution an infinitesimal distance to the west of one edge of the cell to the solution an infinitesimal distance to the west of the edge of the next cell, is then obtained by combining (15) and (17) to give

$$\left.\begin{pmatrix}\tilde{\phi}\\ \Xi\end{pmatrix}\right|_{\tau=1-\epsilon} = \begin{pmatrix}\varphi_1(1) & \varphi_2(1)\\ \mathrm{e}^{\mathrm{i}l\Delta y}\zeta_1(1) & \mathrm{e}^{\mathrm{i}l\Delta y}\zeta_2(1)\end{pmatrix}\left.\begin{pmatrix}\tilde{\phi}\\ \Xi\end{pmatrix}\right|_{\tau=0-\epsilon}. \tag{18}$$

Denote the propagation matrix in (18) as N, and diagonalize it to obtain

$$N = H\begin{pmatrix}K_1 & 0\\ 0 & K_2\end{pmatrix}H^{-1}, \tag{19}$$

where K_1, K_2 are its eigenvalues. Integration over each cell corresponds to multiplying once by the matrix N. Eigenvalues of the propagation matrix can be written as $K_m = \mathrm{e}^{\mathrm{i}\hat{k}_m\Delta x}$, $m = 1,2$, where $\hat{k}_m$ is the zonal wavenumber component. From these eigenvalues K_m, zonal wavenumbers $\hat{k}_m$ are estimated as

$$\hat{k}_m = \frac{ln(K_m)}{\mathrm{i}\Delta x} + \frac{2n\pi}{\Delta x} \quad n = 0,1,2,\ldots \tag{20}$$

The numerical dispersion relation thus has many branches; as $\Delta x \to 0$, the $n = 0$ branch gives the WKB dispersion relation (4). In order to obtain the numerical equivalent of the WKB dispersion relation at fixed frequency, the foregoing procedure is repeated for a range of specified real values of the meridional wavenumber vector component l.

Fig. 3 shows examples of the numerical dispersion relation so obtained (with cubic interpolation) and the corresponding analytical WKB dispersion relation obtained by solving Eq. (4). The lowest branch of the numerical dispersion relation (20) encompasses the range of wavenumbers $|l| < \frac{\pi}{\Delta y}, |k| < \frac{\pi}{\Delta x}$. These limits are set, respectively, by the meridional spacing and the slope of the characteristics. Beyond these bounds, the numerical dispersion relation would be periodic in l and k. The meridional resolution of a Runge–Kutta solution of (6, 7) is indeed limited by the meridional spacing of the characteristics. The zonal resolution of such a solution is however not restricted to the lowest branch of the numerical dispersion relation, but may be much finer because the integration along the characteristics was performed by using an adaptive-step Runge–Kutta method. This enables resolution of waves whose zonal wavenumbers lie outside the zonal limits of the numerical box characterizing the lowest branch of the dispersion relation. In Fig. 3 the higher zonal aliases of the numerical dispersion relation, although resolved in the Runge–Kutta calculation, are plotted folded back into the range $|k| < \frac{\pi}{\Delta x}$.

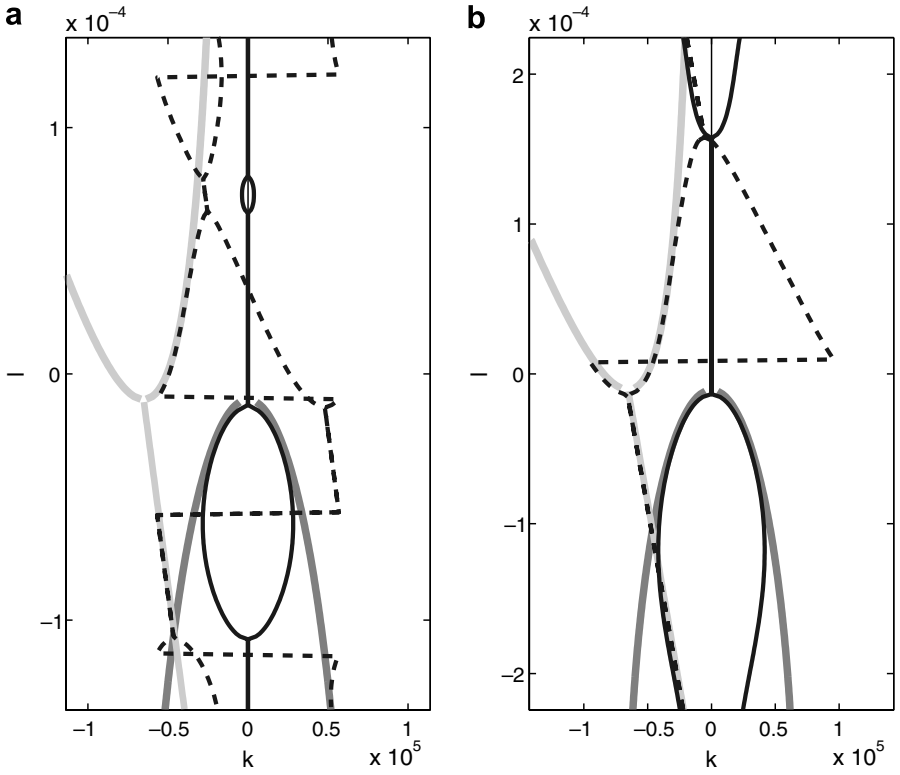

Fig. 3. Numerical and true analytical dispersion dispersion relation at $x = 585$ km, $y = 2171$ km for the solution of Fig. 4. The numerical dispersion relation is obtained by assuming real meridional wavenumber l and evaluating the zonal wavenumber k from (20). The true dispersion relation is similarly obtained from (4). For the true dispersion relation, real values of k are plotted as light gray lines, imaginary values of k are plotted as dark gray lines. For the numerical dispersion relation, real values of k are plotted as dashed lines, imaginary values are plotted as solid black lines. Numerical values of parameters are $U_R = -0.0235$ m/s, $V_R = -.0000712$ m/s, $c = 0.0284$ m/s, $C = 0.0321$ m/s. At this location, with $N = 50$ computational characteristics, the meridional spacing Δy of Y characteristics is $\Delta y = 28$ km (left panel). Right panel: Dispersion relations at the same location as that of the left panel, except with $N = 100$ computational characteristics; $\Delta y = 14$ km. Note the much better numerical resolution of the region of true instability (along most of the negative l axis) in the high resolution right panel than in the low resolution left panel. Note also however the much more extensive aliasing of the numerically resolved region of true instability in the high resolution right panel than in the low resolution left panel.

Fig. 3 illustrates the most important features of the numerical dispersion relation: (i) good agreement with the analytical dispersion relation for small k, l, (ii) preservation of the baroclinic instability which is evident in the analytical dispersion relation at the longer wavelengths, although generally with substantial shrinkage of the most negative part of the range of meridional wavenumbers l over which instability occurs, and (iii) the possible occurrence of new, numerical, small scale instability at the meridional wavenumbers corresponding either to the alias of the numerical reminant of the range of meridional wavenumbers l over which true instability occurs and/or to intersections of the numerically aliased dispersion curves.

5. Discussion

The method of integration along characteristics discussed above has proved useful for the example we studied. In particular, the Matlab adaptive Runge–Kutta routines were able to provide sufficient zonal resolution to avoid the aliased instability, even far into the southwestern part of the subtropical gyre, where the two sets of characteristics tend to be increasingly parallel. Cubic interpolation between the two sets of characteristics was employed, a spline interpolation did not give better results, and both methods were clearly superior to linear interpolation.

The total number of characteristics sets a limit on the meridional resolution. Limited meridional resolution not only results in aliasing of the true instability into high meridional wavenumbers, but also limits the ability of the numerical calculation to resolve the shortest waves. To control both of these difficulties we experimented with smoothing the interpolated fields over three or five adjacent characteristics, effectively adding damping on the right hand sides of (6) and (7). In some cases this worked well, but the true instability was also appreciably damped. Correspondingly Dewar and Huang (2001), solving very similar equations by time-stepping solutions defined on a uniformly spaced horizontal grid, noted persistent small scale variabilty in the southwestern subtropical gyre whose scale was controlled by thickness diffusion, and Dewar (1998) also noted the need for high resolution and/or lateral diffusivity in order to control the short wave part of the solution.

For models with more layers (e.g. Talley, 1985), the solutions generally display a number of geographically distinct ventilated regions, so that it may be difficult to write programs that keep track of the the characteristics and interpolate between them through and across the different flow regions. But even in such cases (particularly including the model of Talley in which the eastern eastern shadow zone is of very small extent compared with that of the present solutions), the central point of this paper – the possible occurrence of small scale numerical instability at wavenumbers corresponding to the alias of the range of wavenumbers over which true instability occurs – is likely to be a difficulty for a variety of numerical schemes.

Although this paper is about numerical matters, a reviewer has suggested that there be some discussion relating the findings of this study to observations. Cerovečki and de Szoeke (in press) provided some elements of such a discussion, but we take the opportunity given by the reviewer to briefly revisit that discussion and comment on some further points raised by the reviewer.

Published studies of the annual component of altimetrically determined sealevel in the subtropical Atlantic and Pacific were not designed primarily to compare the signal over the subtropical gyre with that in its southwestern corner. In the frequency band 0.5–2 cpy Chelton and Schlax (1996) found well defined westward propagation of features in the North Subtropical Pacific altimetric sealevel field accompanied by an increase in amplitude in the western half of the basin. Osychny and Cornillon (2004) found very similar results in the subtropical North Atlantic. But the time-longitude plots of Chelton and Schlax (1996) and the frequency-zonal wavenumber spectra of Osychny and Cornillon (2004) do not allow ready comparison of the signal over the gyre with that in its southwestern corner. Osychny and Cornillon (2004) do map the variabilty in the period band 4 years to 3 months over the north Altantic subtropical gyre, but their map is dominated by the decay of variance eastward away from the Gulf Stream and so does not clearly display the spatial variation – if any – of sealevel variance in the southwestern part of the gyre. Roemmich and Gilson (2001) similarly map the rms variability of altimetrically determined sealevel in the North Pacific subtropical gyre over a seven year period. They find a clear maximum near to and eastward of the Kuroshio, qualitatively like that of Osychny and Cornillon (2004) near the Gulf Stream, and also find a strong secondary maximum at about 20° N extending eastward from the western boundary towards Hawaii.

It is tempting to associate this last feature with the westward growth found in the present two-and-a-half layer model solutions, but as one adds layers (e.g. Talley, 1985) the solutions rapidly become much more complex and in particular the meridional extent of the eastern eastern shadow zone (within which the present instability manifests itself in the two-and-a-half layer solutions) becomes very small in the western part of the gyre. Without further detailed analysis it is not clear how this will change the stability properties of the flow there. A different point is that, when annual period internal Rossby wave rays are propagated westward away from realistically shaped coasts but without steady background flow or bottom relief in the Pacific (Schopf et al., 1981), they tend to refract equatorward sufficiently rapidly that they do not reach the southwestern corner of the subtropical gyre. It is difficult to predict how mean flows in a model such as the present two-and-a-half layer one or more complex mean flows will modify this effect, but the important result is that coastal shape may play an important role in helping/hindering wave refraction into the far western corner of the gyre.

The most important point of this paper remains that, if the coupled wave instability of the two-and-a-half layer model is found in a more complex model, then the numerical problems noted here will very likely be met in numerical solution of that model.

6. Conclusions

For model flows typical of the eastern shadow zone of a two-and-a-half layer model subtropical gyre, annual period long wave perturbations are generally baroclinically unstable for a range of meridional wavenumbers l (Walker and Pedlosky, 2002, elucidated the important destabilizing effect of non-zonal background flow; Cerovečki and de Szoeke, 2005, in press, explicitly considered subtropical gyre background flow). Outside this range there are two independently propagating long Rossby waves (the A and N modes of Liu, 1999a) whose dispersion plots in the zonal-meridional k, l wavenumber plane approach one another as the meridional wavenumber approaches the unstable range.

Cerovečki and de Szoeke (in press) show that for annual period perturbations in a rectangular basin that are generated by an annual period wind stress that is smooth at basin scales, the instability manifests itself in the far southwestern region of the subtropical gyre in the following way. As long waves propagate westward in the eastern shadow zone of the model subtropical gyre, they tend to refract so that the meridional wavenumber increases towards more positive values (the line of crests tends from being nearly meridional near the eastern boundary to trending southwest-to-northeast near the western boundary of the eastern shadow zone), but the upper bound of the range of meridional wavenumbers for which annual period solutions are unstable (Fig. 1) rises towards positive values as the location at which the dispersion relation is evaluated is moved towards the southwest: the refraction is sufficiently slow that westward propagating waves eventually enter a region in which their meridional wavenumber lies within the unstable range of meridional wave numbers, and westward growth of the solution occurs.

As noted above and as illustrated in Fig. 3, when solving the perturbation problem numerically, numerical deformation of the dispersion plots of these long Rossby waves in the k, l plane results (i) in appreciable truncation of the range of meridional wavenumbers corresponding to the true instability, so that the range of meridional wavenumbers for which instability occurs does not extend to values as negative as for the true instability, (ii) in aliasing of the the most negative portion of the numerically truncated range of instability into a generally positive range of meridional wavenumbers which gives rise to a numerical instability characterized by meridional wavenumbers generally corresponding to much smaller meridional scales than those of the true instability, and sometimes (iii) in aliasing of the wave dispersion plots in such a way that additional regions of close approach in addition to the one corresponding to the true instability occur.

These effects can give rise to the seemingly paradoxical situation illustrated in Fig. 4. The top panel of this figure shows the numerical solution of (6) and (7) with an eastern boundary condition that makes the eastern boundary ratio of ξ_1 to ξ_2 such as to give rise to long waves. The numerical resolution is coarse, the total number of N of zonal and of tilted characteristics is 30, but the solution correctly restricts the region of westward growth to the far southwestern corner of the eastern shadow zone of the subtropical gyre. Increasing N should improve the resolution and lead to a more accurate solution, but instead for $N = 100$ (bottom panel, Fig. 4), an incipient numerical instability at much shorter meridional scales than those of the unstable region of the

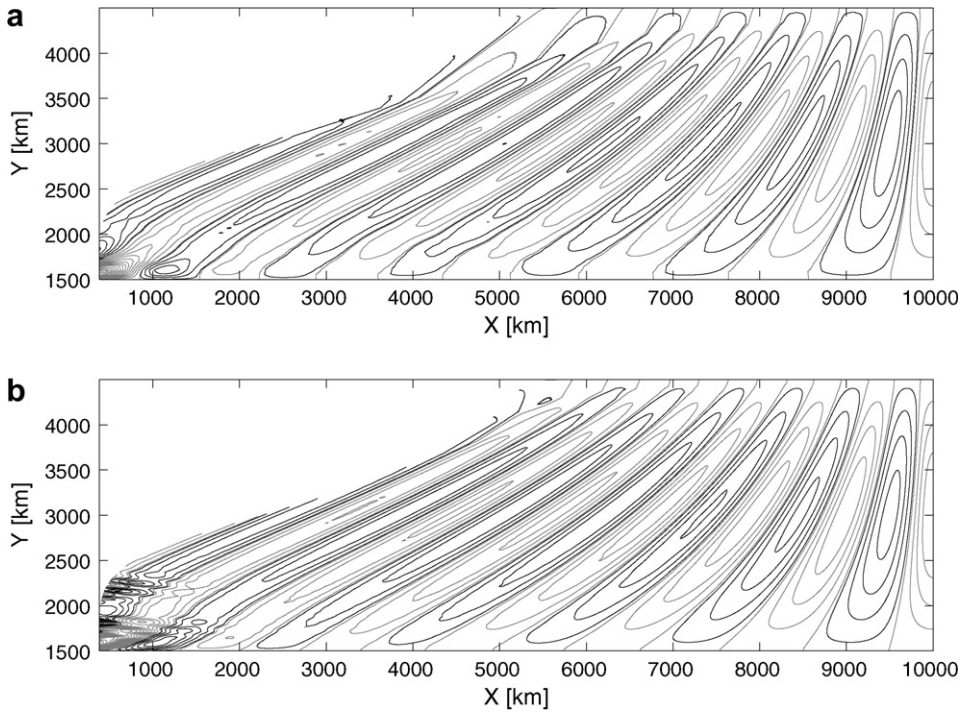

Fig. 4. Top panel: Snapshot of the annual period interfacial displacement ξ_2 of the base of the middle layer obtained by solving (1) with no forcing but with an eastern boundary condition that sets the meridional wavenumber at π/Δ and sets the ratio of ξ_1 to ξ_2 at the eastern boundary to generate only the long wave free solution. The background steady flow is specified by the parameters $H_{10} = 300$ m, $H_{20} = 750$ m (undisturbed interfacial depths at the eastern boundary), $\gamma_1 = 0.0245$ m/s^2, $\gamma_2 = 0.01$ m/s^2 (see text) and is driven by the steady Ekman pumping described in the caption of Fig. 1. The numerical integration is carried out along $N = 30$ y and Y characteristics. Note unstable westward growth of the solution in the far southwestern part of the basin. Contour interval is 0.25 m from -1.3 m to 3.4 m. Light (dark) contours indicate negative (positive) displacements. Bottom panel: The same, except for $N = 100$ y and Y characteristics. Although the numerical resolution of the bottom panel is substantially improved relative to that of the upper panel, incipient instability in the southwestern part of the domain is more evident in the more highly resolved solution of the bottom panel than in the relatively poorly resolved solution of the top panel. Contour interval is 0.25 m from -2.6 m to 4 m.

top panel is clearly visible. The manner in which this comes about may be understood by examining the manner in which changing the resolution changes the numerical dispersion relation; this is illustrated in Fig. 3.

If the meridional resolution is rather coarse (Fig. 4a), then the range of meridional wavenumbers corresponding to the true instability is so severely truncated that this truncated range is not aliased into a range of positive meridional wavenumbers corresponding to numerical instability. Only a very small region of numerical instability resulting from crossing of the aliased dispersion curves is present. The result is that the coarse resolution numerical solution displays the true instability in the southwestern part of the subtropical gyre with moderate distortion corresponding to truncation error. As the meridional resolution is increased (Fig. 4b), the numerical truncation of the true instability range is decreased so that the range of wavenumbers into which that range is aliased is increased; the result is the seemingly paradoxical appearance of spurious small scale numerical instabilities in the far southwestern part of the subtropical gyre as the resolution is increased.

Finally, it is important to note that the numerical phenomena noted above also may occur in more complicated models and/or with other finite difference numerical procedures. Thus, for example, if the solutions of (1) are made discrete on a rectangular "x, y" grid, and the single y derivative in (1) is replaced by a finite difference approximation, then (1) become a set of coupled equations that may be integrated westward in x using, for example, the Runge–Kutta procedure. If the meridional gridspacing is Δy, then the numerical equivalent of (4) is simply

$$\sigma^2 + \sigma(c + C)k - CU_{\mathrm{R}}k^2 - CV_{\mathrm{R}}k\sin(2l\Delta y)/(2\Delta y) = 0. \tag{21}$$

It is immediately clear that the entire dispersion plot is periodic in l with period $\pi/\Delta y$, so that there will again be an alias into positive l of the numerically modified region of true instability that is usually confined to a negative range of l for $V_R < 0$.

Acknowledgements

This work was supported by the National Science Foundation through Grants OCE-9907008 and 0220471. IC would like to thank William Dewar for motivating and insightful discussions as well as two anonymous reviewers whose comments materially improved the paper.

References

Cerovečki, I., de Szoeke, R.A., 2005. Initially forced long planetary waves in the presence of nonzonal mean flow. J. Phys. Oceanogr. 36, 507–525.

Cerovečki, I., de Szoeke, R.A., in press. How purely wind-driven long PG waves may be energized in the western part of ocean subtropical gyres. J. Phys. Oceanogr.

Chelton, D.B., Schlax, M.G., 1996. Global observations of oceanic Rossby waves. Science 272, 234–238.

Dewar, W., 1998. On "Too Fast" baroclinic planetary waves in the general circulation. J. Phys. Oceanogr. 28, 1739–1758.

Dewar, W., Huang, R., 2001. Adjustment of the ventilated thermocline. J. Phys. Oceanogr. 13, 293–309.

Kubokawa, A., Nagakura, M., 2002. Linear planetary wave dynamics in a 2.5-layer ventilated thermocline model. J. Mar. Res. 60, 367–404.

Liu, Z., 1999a. Planetary wave modes in the thermocline: Non-Doppler-shift mode, advective mode and Green mode. Quart. J. Roy. Meteor. Soc. 125, 1315–1339.

Liu, Z., 1999b. Forced planetary wave response in a thermocline gyre. J. Phys. Oceanogr. 29, 1036–1055.

Luyten, J., Pedlosky, J., Stommel, H., 1983. The ventilated thermocline. J. Phys. Oceanogr. 13, 293–309.

Osychny, V., Cornillon, P., 2004. Properties of Rossby waves in the North Atlantic estimated from satellite data. J. Phys. Oceanogr. 34, 61–76.

Pichevin, T., 1998. Baroclinic instability in a three layer flow: a wave approach. Dyn. Atmos. Oceans 28, 179–204.

Roemmich, D., Gilson, J., 2001. Eddy transport of heat and thermocline waters in the North Pacific: a key to interannual/decadal climate variability? J. Phys. Oceanogr. 31, 675–687.

Sakai, S., 1989. Rossby–Kelvin instability: a new type of ageostrophic instability caused by a resonance between Rossby waves and gravity waves. J. Fluid Mech. 202, 149–176.

Schopf, P., Anderson, D., Smith, R., 1981. Beta-dispersion of low-frequency Rossby waves. Dyn. Atmos. Oceans 5, 187–214.

Stoker, J.J., 1957. Water Waves. Interscience Publishers, pp. 567.

Talley, L., 1985. Ventilation of the subtropical North Pacific: the shallow salinity minimum. J. Phys. Oceanogr. 15, 6333–6649.

Walker, A., Pedlosky, J., 2002. Instability of meridional baroclinic currents. J. Phys. Oceanogr. 32, 1075–1093.